J. Fluid Mech. (1975), *vol.* 72, *part* 4, *pp.* 695–719
Printed in Great Britain

The electron-beam fluorescence technique for measurements in hypersonic turbulent flows

By JEROME A. SMITH AND JAMES F. DRISCOLL†
Gas Dynamics Laboratory, Princeton University, Princeton, New Jersey

(Received 16 December 1974 and in revised form 13 June 1975)

The electron-beam fluorescence technique has been employed in measuring simultaneous density and temperature fluctuations in a hypersonic ($M \simeq 16$), adiabatic wall boundary layer. The paper discusses this technique, as it is applied to the conditions of relatively high density associated with turbulent flows. It presents general considerations concerning the attainable frequency response and spatial resolution of the technique. It describes results from initial measurements in a boundary layer on a wind-tunnel wall. These results show that the r.m.s. of the density, temperature and pressure fluctuations are large, much larger than observed in supersonic boundary layers.

1. Introduction

Reported measurements of fluctuating quantities in hypersonic ($M \gtrsim 9$) turbulent boundary layers are scarce indeed. In the past few years, results from hot-wire measurements by Laderman & Demetriades (1974), Kemp & Owen (1972) and Fischer *et al.* (1971) at edge Mach numbers of 9·4, ~ 40, and 20, respectively, have been reported. These investigations demonstrate the difficulties of obtaining statistical information on the fluctuating flow variables. Not only is it relatively difficult to generate hypersonic flow with the high unit Reynolds number necessary for fully-developed turbulent shear flows, but it takes a great deal of effort to perform the measurements and data analysis. The high flow velocity and the effects of compressibility combine to place great demands on frequency response, and require multiple simultaneous or serial measurements.

The requirements induced by compressibility are by far the most difficult to deal with. The signal amplitude of almost any probe one can envision varies with the local fluid number density in the sampled volume (i.e. the number of information carriers present), be it an optical 'probe', hot wire, Pitot probe or other. In addition, the signal amplitude is usually a function of at least one other flow variable of interest, a function of the form of a product with number density. Consider first the relatively simple case of a probe which is responsive to a product of number density and one other flow property. When the average number-density variations are small (as is the case in many subsonic flows), one can

† Present address: Department of Aerospace Engineering, University of Michigan, Ann Arbor, Michigan.

determine the other flow property's mean from the mean of the signal directly. Furthermore, statistical information about the other flow property can be obtained by direct statistical analysis of the output signal. In flows with variable mean density, when fluctuations are small, one can also determine the mean of the other flow property from the mean of the signal, by arguing that the mean of the product is equal to the product of the means. That is, knowing the mean density at the point of interest, and the functional dependence of the signal on the other flow property of interest, permits one to calculate the mean of the other flow property from the mean signal. Determining the nature of the fluctuations requires more sophistication; but a linearized analysis, coupled with measured influence coefficients, suffices to determine most of the information of interest about this other flow property.

In hypersonic shear layers, neither the average number-density variations nor the turbulent number-density fluctuations are small (e.g. Laderman & Demetriades 1974). Mean flow properties may not be determined from the mean signal amplitude, since the product of the means may no longer be assumed to equal the mean of the product. (Even if the probe response is dependent on but one flow variable, it may not be possible to determine the mean of that flow property directly from the mean of the signal, when the probe response has a non-linear dependence and fluctuations are large.) In this situation, when the probe response is dependent on more than a single flow property, it is necessary to measure a set of signals simultaneously, so that instantaneous values of the flow properties can be computed before performing any statistical analyses. In other words, it is much less likely, for hypersonic turbulent flows, that direct statistical analysis of probe output can be used to deduce the nature of the turbulent fluctuations of a particular flow variable.

We have developed a technique which provides *simultaneous* measurements of number density and temperature with megahertz frequency response. The results from this technique, coupled with an appropriate equation of state, permit one to determine the time variation of all the thermodynamic state variables. This paper contains a general discussion of the application of the electron-beam fluorescence technique to the measurement of turbulent fluctuations, and we present some initial measurements of density, temperature, and pressure fluctuations in an adiabatic wall, hypersonic ($M \sim 16$), tunnel-wall boundary layer.

2. The electron-beam fluorescence technique for high-density flows

The principle of operation of the electron-beam fluorescence technique is rather simple. A small-diameter beam of high-energy electrons passing through a gas creates, by inelastic collisions, a small fraction of excited or ionized atoms or molecules. Radiation of multiple wavelengths in the vicinity of the beam is then given off in the process of de-excitation or recombination. The intensity of the radiation is always dependent on the electron-beam current (i.e. the number of electrons in the primary beam per second). The intensity may also be dependent on the number density and the temperature of the gas, the energy of the primary electrons, and the relative concentration of the different species, if any, that

comprise the gas. By measuring the intensity variation along the beam, one can determine many flow variables of interest. An excellent summary of the development and application of the electron-beam fluorescence technique for the measurement of various flow properties has been written by Muntz (1968). This reference contains a discussion of the underlying principles of the electron-beam fluorescence technique, and an extensive bibliography of related papers published up to the end of 1968.

Use of the electron-beam fluorescence technique for the measurement of turbulent fluctuations was first demonstrated by Boyer & Muntz (1967) in a $M = 12{\cdot}6$ nitrogen flow, and subsequently in a $M \sim 8$ air flow by Wallace (1968). In both of these investigations, flows were provided by shock tunnels with observation times limited to a few milliseconds. Mean density and r.m.s. density fluctuation profiles were presented for a 10° half-angle cone wake by Boyer & Muntz (1967), and for a nozzle wall boundary layer by Wallace (1968). Although the influence of gas temperature fluctuations was present in each study, these effects were suppressed by appropriate choice of operating conditions and/or by the use of some simplifying assumptions in the data reduction scheme. Since the effects of temperature variations were always present for the conditions of the present study, and since the effects of temperature are usually present at the relatively high densities associated with turbulent flows, attention in this paper is focused on the dependence of intensity, generated by an electron beam, on density *and* temperature variations.

2.1. *Fluorescence intensity dependence*

In general, for constant electron-beam operating conditions, one can relate the dependence of the intensity of a spectral line (or band) on the gas density and temperature by equating the production rate to the depletion rate of the population of the upper level of an observed atomic or molecular transition. Muntz (1968) derived such an equation, which has essentially the same form as a Stern–Volmer quenching equation (Mitchell & Zemansky 1971), i.e.

$$I_{ul} = \frac{k_1 n}{1 + k_2 n Q(T) \{(8/\pi) RT\}^{\frac{1}{2}}}. \tag{1}$$

(k_1 and k_2 are constants; n is the number density; T is the temperature; R is the gas constant; Q is the total collision quenching cross-section for the upper level u; and I_{ul} is the intensity of the observed transition from an upper level u to a lower l.) This equation is derived assuming electron-beam current and accelerating potential are constant; otherwise, k_1 would not be a constant. Physically, k_1 is the ratio of the excitation rate, arising from primary and secondary electron inelastic collisions, to the total spontaneous decay rate for the upper level. The second term in the denominator is the ratio of the rate of depopulation, due to atomic or molecular collisions, to the total spontaneous decay rate for the upper level (i.e. k_2 is the inverse of the total spontaneous decay rate). The collision cross-section Q is assumed to be temperature-dependent, and represents, in essence, the cross-section for depopulation of the upper level by ground state atoms or molecules.

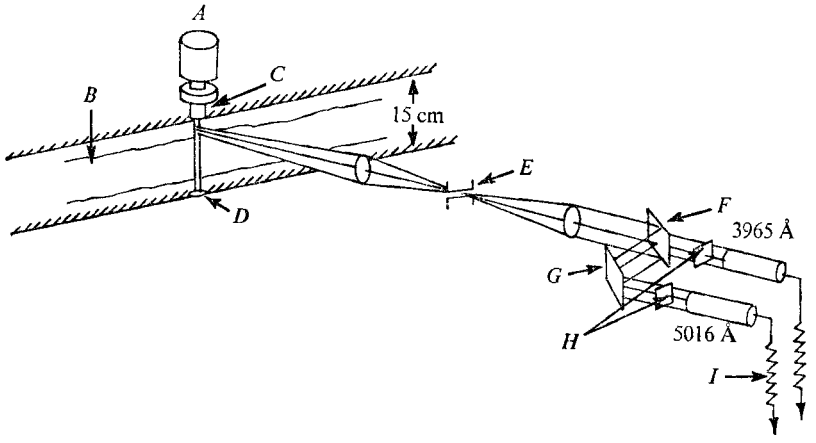

FIGURE 1. Schematic of apparatus for measuring intensity. *A*, electron gun assembly; *B*, boundary layer; *C*, drift tube; *D*, Faraday cup; *E*, adjustable slit; *F*, dichroic beam splitter; *G*, mirror; *H*, narrow-band interference filters; *I*, load resistors.

Previous use of the electron-beam fluorescence technique has been, for the vast majority of cases, limited to conditions in which the second term in the denominator is much smaller than unity. In this situation, observed intensity is linearly related to number density. This quenching term in the denominator will seldom, if ever, be negligible at the number densities associated with turbulent flows. That is, collision-quenching cross-sections are seldom that small, nor are spontaneous decay rates that large. Of course, in the limit of very high number densities (efficient collision quenching), the intensity is solely a function of temperature. Therefore, only if collision quenching is completely dominant for an observed transition, will measuring the intensity variations of a single line be sufficient to determine the spatial or temporal variations of a single gas property. This sensitivity to more than a single gas property is similar to the problems encountered using a hot wire in compressible turbulent flows, mentioned above. However, if two line intensities, whose intensity variations are described by an equation like (1), but with different values for k_2 and $Q(T)$, can be measured simultaneously, the density and temperature can be determined at each instant of time. In § 3 the results of our calibration of two lines in helium are shown; and there follows an assessment of the spatial resolution, frequency response, and signal-to-noise ratio of the technique.

It should be noted that Boyer & Muntz (1967) accounted for the temperature dependence in the observed intensity fluctuations of the light emitted from the 0–0, 0–1, and 0–2 first negative bands in nitrogen by measuring the relative sensitivity of intensity variations to number-density variations at appropriate temperatures. Since this was roughly constant over the temperature range of interest, and since they assumed small perturbations, all intensity fluctuations were multiplied by a factor of 1·3 ,to give number-density fluctuations directly. Wallace (1968), on the other hand, ignored temperature effects. Working at lower number densities ($n \leqslant 7 \times 10^{16}\,\mathrm{cm}^{-3}$) in air, he observed an essentially linear dependence of intensity (3600–4600 Å) on number density at room temperature, the only temperature for which an independent calibration was made.

3. Calibration results for helium flows

The apparatus shown schematically in figure 1 was used to measure intensities of various helium lines for various flow conditions in the test section of a helium wind tunnel. The primary electron beam had an accelerating potential of 20 keV, and the beam current varied from 0·10 to 2·0 mA. Tests were conducted to verify that intensity for each of the lines varied linearly with beam current over this range. The beam passed vertically through the full width of the test section, and was collected on the opposite wall with a 5 cm diameter Faraday cup connected to earth by the microvolt ammeter that monitored beam current. A pair of turning mirrors and a field lens were used to collect light at an angle of 27° from the horizontal. (Viewing from this angle was required to observe the intensity in the bottom of the tunnel-wall boundary layer. However, for the calibration procedure, measurements were made only in the free stream.) The field lens had a 5 cm diameter with a focal length of 15 cm. Light from the beam was focused on a 1 cm wide slit with variable height. For calibration and boundary-layer measurements, the slit height was set at 1·5 mm, with the image of the slit lying in a horizontal plane, perpendicular to the primary beam. One-to-one magnification was employed throughout. Light passing through the slit was collimated and split with a dichroic beam splitter. The beam splitter was coated, to give 90 % transmission for wavelengths less than 4500 Å, and 85 % reflexion for wavelengths greater than 4500 Å. This provided more signal than a conventional 50–50 beam splitter. Light from the beam splitter then passed through a pair of narrow-band interference filters, and focused on the photocathodes of separate EMI 9524S photomultiplier tubes. (During the calibration procedure, the beam splitter was removed, and the appropriate interference filter was placed in the active optical path.)

The current of the photomultiplier tubes passed through a load resistor, and the voltage across the load resistor was used as a source for X–Y plotters, oscilloscopes, spectrum analyzers, tape recorders or correlators, depending on the information sought. The magnitude of the load resistor plays an important role in determining the ultimate frequency response and signal-to-noise ratio of the technique. In our case, a 2000 Ω load resistor provided a frequency response of 2 MHz with $S/N \sim 10$, but owing to other limitations on frequency response (to be discussed below), a 15 kΩ load resistor was employed in the measurement of turbulent fluctuations.

The entire optical assembly was mounted on a milling-machine base, which could be made to traverse along both the beam and the flow axis of the wind tunnel. The position of the slit image, with respect to the tunnel wall and the centre of the electron beam, could be determined to within 0·05 mm by dial indicators and/or linear transducers, monitoring movement of the milling-machine translation stages with respect to the base. For studies of the axial extent of radiation, the slit image was turned 90°, so that its width lay along the primary beam, and its height was reduced to 0·125 mm. To minimize beam spreading, all measurements were made within 4 cm of the electron-beam source in the side wall.

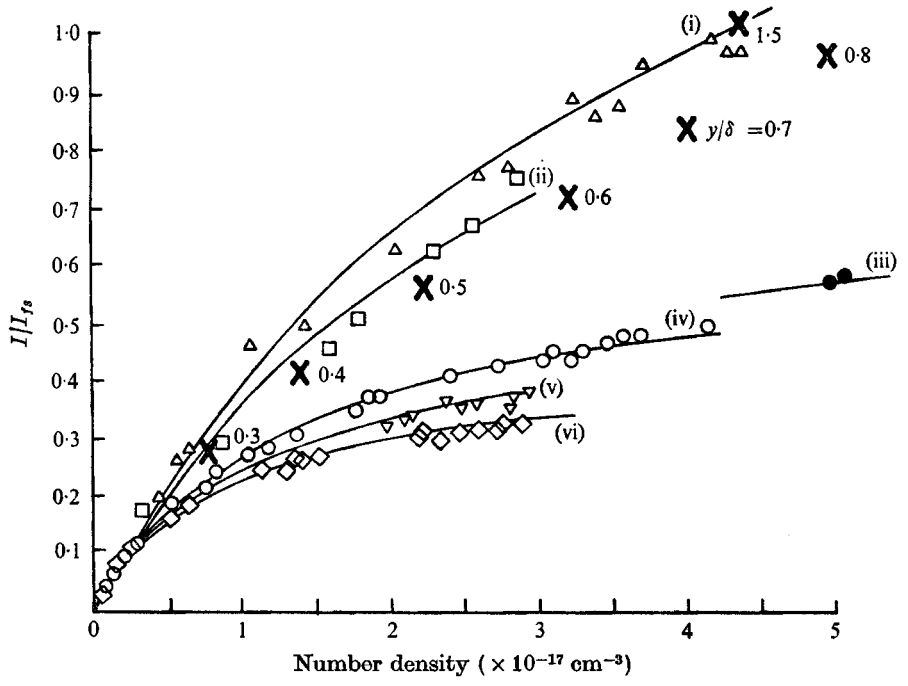

FIGURE 2. Calibration curve of intensity as a function of density and temperature, for the 5016 Å line. ×, boundary-layer conditions deduced from Pitot surveys.

	(i)	(ii)	(iii)	(iv)	(v)	(vi)
Temperature (°K)	3·5	9·0	60·0	100·0	200·0	300·0

To determine the variation of line intensity with number density and temperature, a small free-jet facility was used, in addition to the wind tunnel described above. A greater variety of supply pressures and nozzle geometries were available in the free-jet facility, which provided a wide range of number-density and temperature conditions. The optical assembly and electron-beam operating conditions were kept the same in both facilities, and the range of conditions available in each facility overlapped, so that no dependence upon absolute intensity measurement was required.

Number density and temperature at a point were determined by measuring Pitot pressure there. In conjunction with the measured stagnation temperature and pressure, Pitot pressure could be used to calculate all the flow properties from the isentropic flow relations. This flowing-gas calibration technique is felt to be superior to a calibration obtained with a 'controlled bleed' or static test chamber, for two reasons. First, using the wind-tunnel and free-jet facilities more nearly simulates the actual measurement conditions. Errors in calibration, arising from multiple-collision effects, are less likely to be made. Second, the high mass-flow rate associated with the wind tunnel, pumped by a steam ejector, and free-jet facilities assures one that the purity of the gas will be essentially that of the source, always less than 20 p.p.m. for the helium used in these tests. In a static chamber, the impurities are typically hundreds or thousands of p.p.m. (In a static chamber, the ratio of the lowest pressure attainable to the operating pressure does

	c_1	c_2	α
5016 Å(3^1P-2^1S)	$5{\cdot}03\times10^{-18}$	$1{\cdot}83\times10^{-18}$	0·33
3965 Å(4^1P-2^1S)	$15{\cdot}5\times10^{-18}$	$8{\cdot}55\times10^{-18}$	0·35

n in atoms cm^{-3}, T in degrees Kelvin

TABLE 1

not give the impurity level. The impurity level must be determined from the characteristics of the particular vacuum system employed.) Impurities are important, because they can have a different collision quenching cross-section from the pure gas. For example, we found a difference of 15–20 % in intensity of the 5016 Å ($3^1P\rightarrow 2^1S$) line at room temperature, at number densities of the order of 10^{17} cm^{-3} (a few Torr), depending on whether we used a mechanical vacuum pump and a controlled helium bleed, or the steam ejector and a substantial subsonic helium flow. Since the intensity observed in the controlled-bleed case was always lower, we conclude that the quenching cross-section for air, on the 3^1P state of helium, is greater than pure helium.

3.1. *Calibration of the* 5016 Å *line*

Initially, a calibration of the 5016 Å ($3^1P\rightarrow 2^1S$) line was undertaken. This line was used extensively for measuring number densities in relatively low-density ($n \lesssim 2\times10^{16}$ cm^{-3}) helium flows, since it is the most intense. Its intensity varies linearly with number density for 10^{15} cm$^{-3} < n < 3\times10^{-16}$ cm^{-3} (cf. Muntz 1968; St John, Bronco & Fowler 1960; Hunter 1972). Shown in figure 2 is the variation of intensity over a wide temperature and number-density range. As a result of these measurements, we found that (1) could be simplified to

$$\frac{I}{I_{fs}} = \frac{c_1 n}{1+c_2 n T^{\alpha}}. \tag{2}$$

(I_{fs} is the intensity measured for $T = 3{\cdot}5\,^{\circ}$K, $n = 4{\cdot}9\times10^{17}$ cm^{-3}, $i_b = 2{\cdot}0$ mA and $V_b = 20$ keV.) The values of c_1, c_2 and α are given in table 1. c_1 and c_2 were determined by a least-squares fit to the data for various trial values of α. The value of α which gave the minimum standard deviation was then used in (2). The magnitude and temperature dependence of the effective collision-quenching cross-section Q in (1) was determined from these data. Comparing (1) and (2),

$$Q_i = \frac{c_2 T^{\alpha-\frac{1}{2}}}{(8/\pi)Rk_2} = \frac{c_2 T^{\alpha-\frac{1}{2}}\sum_j A_{ij}}{(8/\pi)R}. \tag{3}$$

The sum of spontaneous decay rates used to calculate Q_{3^1P} excluded the rate for transitions to the ground state ($A_{3^1P\rightarrow 1^1S}$), since this radiation is trapped for these relatively high number densities (Maguire 1967). Values for $A_{3^1P\rightarrow 2^1S}$ and $A_{3^1P\rightarrow 3^1S}$ were taken from Massey & Burhop (1969). Using the latter and the measured values of c_2 and α, we find

$$Q_{3^1P} = 3{\cdot}43\times10^{-15}(T)^{-0{\cdot}17}\ \text{cm}^2 \tag{4}$$

(T is in °K). These values agree fairly well with the calculated results of Hunter (1972); but they are approximately a factor of two larger than his measured value at 22 °K, and slightly smaller than his value at 300 °K. Hunter did not observe the relatively weak temperature dependence found in this study. This result implies that the 5016 Å line intensity varies essentially as $T^{-\frac{1}{2}}$ at high densities.

The curves in figure 2 correspond to solutions of (2) plotted for various fixed temperatures. The measured points do not all fall on the curves, because the measured temperatures do not all correspond exactly to those for which curves are plotted. The accuracy of these data is approximately $\pm 3\,\%$. The crosses in figure 2 indicate the locus of points in the turbulent tunnel-wall boundary layer that we wished to investigate. Details of the boundary-layer conditions will be discussed later. It is clear from figure 2 that, except very near the wall, the intensity of the 5016 Å line is dependent on both temperature and density. Therefore, another line exhibiting different quenching characteristics was found, so that density and temperature could be determined simultaneously in a small volume of the flow.

3.2. *Calibration of the* 3965 Å *line*

Studies of fluorescence generated by an electron beam for other lines in helium have been conducted by Hilliard, Ocheltree & Storey (1970), Maguire (1967), and Muntz & Marsden (1963). The first was most revealing for present purposes, since it was performed in a high-speed flow; and it demonstrated that fluorescence from many of the helium lines emanates from points far outside the primary beam-excitation region, making them unsuitable. After an examination of the spatial distribution and temperature dependence of several helium lines, it was found that the 3965 Å ($4^1P \rightarrow 2^1S$) line intensity provided adequate spatial resolution and greater temperature sensitivity than the 5016 Å. Details of this search for a suitable second line are given by Driscoll (1975).

Using the procedure described earlier, we determined the intensity dependence of the 3965 Å line on density and temperature variations. The results are shown in figure 3; and one can observe the relatively greater effect of quenching. This is the result of both a smaller spontaneous transition probability, and a larger collision-quenching cross-section. Equation (2) was found adequately to represent the observed intensity variation. The appropriate values of c_1, c_2 and α, determined from a least-squares fit to these data, are given in table 1. The effective collision-quenching cross-section Q_{4^1P} was determined from (3), with the appropriate constants. Again the spontaneous transition probability $A_{4^1P-1^1S}$ was ignored, because all the radiation from this transition is trapped and subsequently removed by other radiative or collisional processes. The results in figure 3, with (3), yield

$$Q_{4^1P} = 9{\cdot}78 \times 10^{-15}(T)^{-0{\cdot}15}\ \mathrm{cm}^2. \tag{5}$$

(T is the temperature in °K.) This cross-section is approximately three times larger than Q_{3^1P}; and it has a slightly different temperature dependence, although the difference between 0·15 and 0·17 is hardly discernible over this temperature range (3·5 °K $\leqslant T \leqslant$ 300 °K).

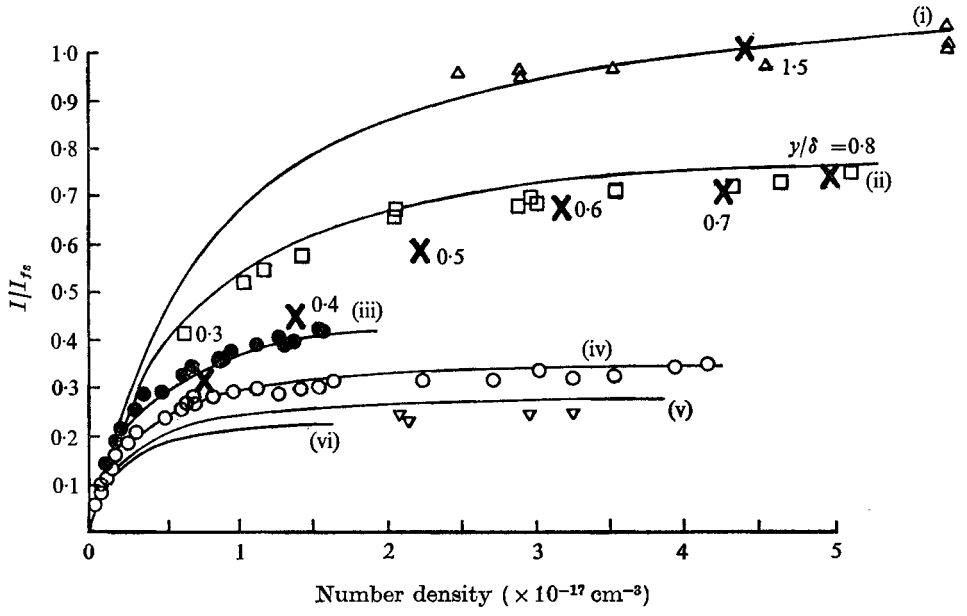

FIGURE 3. Calibration curve of intensity as a function of density and temperature, for the 3965 Å line, ×, boundary-layer conditions deduced from Pitot surveys.

	(i)	(ii)	(iii)	(iv)	(v)	(vi)
Temperature (°K)	3·5	9·0	47·0	100·0	200·0	300·0

Comparing the values of c_2 in table 1 for the two lines, one can see that the collision-quenching term is five times larger, at a given flow condition, for the 3965 Å line than that for the 5016 Å line.

The intensity of the 3965 Å line is approximately one-seventh of that of the 5016 Å line (cf. Muntz & Marsden 1963); but there is still sufficient intensity for good statistical accuracy. The loci of the mean values of density and temperature at various points in the boundary layer are also shown in figure 3. It can be seen that any variations in intensity of this line are much more the result of temperature fluctuations than density fluctuations.

4. Frequency response and spatial resolution

The two calibration curves, figures 2 and 3, and the knowledge that the observed radiation emanates from a region close to the primary excitation zone, are sufficient to determine mean values of density and temperature in a small volume. However, several questions concerning frequency response, spatial resolution, and signal-to-noise ratio had to be answered before this became a viable technique for measuring turbulent fluctuations.

Tests were made with the apparatus used for calibration shown in figure 1. One of the hypersonic helium wind tunnels at the Gas Dynamics Laboratory, designated He-2, was used for this study. For stagnation conditions of 300 °K and 15·3 atm, free-stream conditions were $M = 16{\cdot}3$, $n = 4{\cdot}9 \times 10^{17}$ cm^{-3}, $T = 3{\cdot}5$ °K, with a unit Reynolds number of $5{\cdot}1 \times 10^4$ cm^{-1}. Measurements were

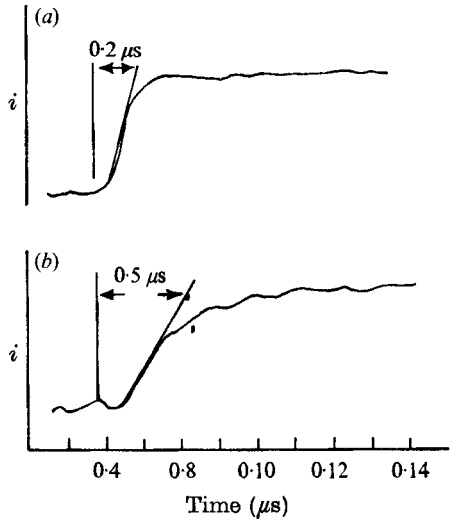

FIGURE 4. Rise time of the optical system. $R_L = 2$, $C_L = 250$ p.f. (*a*) Beam pulse. (*b*) Photomultiplier.

made in the wall boundary layer and free stream at a point in the test section approximately 82 cm downstream of the nozzle throat. We examined three factors that determine the effective bandwidth of this technique: (i) the bandwidth of the detectors; (ii) the spatial extent of the collected light; (iii) the bandwidth of the recording apparatus.

4.1. *Detector response*

The frequency response of the detection optics–photomultiplier assembly was checked by electrostatically deflecting the electron beam across the entrance aperture in the side wall. The results of such a test appear in figure 4, where reproductions of oscillograms are shown. The upper trace represents the time history of the beam current as it was switched on; the lower trace shows the corresponding response from the photomultiplier tube measured across a 2 kΩ load resistor. This load resistor provides a maximum bandwidth of approximately 2 MHz. Subsequent measurements were made with a 15 kΩ load resistor, which enhanced the signal-to-noise ratio, since other factors (to be described) limited the effective bandwidth of the technique to 300 kHz.

4.2. *Beam spreading effects*

The spatial extent of the fluorescent region sampled can be the limiting factor determining the effective bandwidth of this technique. That is, spatial fluctuations with a wavelength equal to the sampled fluorescent region diameter d will not be resolved, or in terms of frequency response

$$f_{\max} \cong U/d. \tag{6}$$

(U is the mean flow velocity.) Since the fluorescent region is essentially cylindrical, it is of no benefit to aperture the collecting optics so that a region smaller

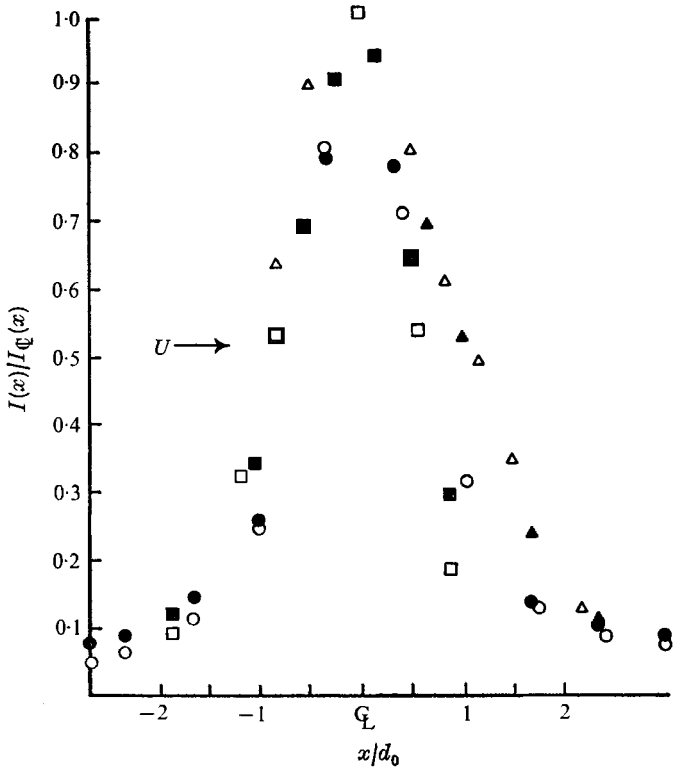

FIGURE 5. Axial extent of the radiation from the 5016 (open symbols) and 3965 Å (closed symbols) lines. Slit height $\frac{1}{8}d_0$, $d_0 = 0{\cdot}75$ mm. Beam intensity profile at y (cm): ○, 0·762; □, 2·54; △, 3·81.

than the beam diameter is sampled. Thus, the length d in (b) may be thought of as the fluorescent region diameter for the particular spectral line under investigation. A practical limit for d is 1 mm, and for supersonic helium flows emanating from a room temperature plenum $U \simeq 2\,\text{mm}\,(\mu\text{s})^{-1}$, implying $f_{\max} \simeq 2\,\text{MHz}$. Beam diameters of a few mm are often found in practice, thus restricting the order of $f_{\max}$ to 0·5 MHz.

Ideally one would like to have the spatial and temporal resolution determined by the initial beam diameter (i.e. the diameter of the hole from which the beam emanates). However, under certain circumstances, radiation is often observed at significant distances from the primary beam, a feature that lends itself to flow visualization, but not point measurements. There are several causes of this apparent beam spreading. (i) Primary electrons, scattered by elastic collisions, can produce radiation outside the initial beam diameter. (ii) Secondary electrons, created by ionizing collisions of the primaries, while small in number, have large inelastic cross-sections compared with that of the primary electrons; and they may be emitted at large angles to the primary beam. (iii) Resonance radiation trapping, which arises when the upper level of the transition being investigated has an optically-allowed transition to the ground state, creates a situation in which emitted radiation may be absorbed, re-emitted, etc., and thus be diffused.

(iv) The excited-state lifetime may be so long that the excited atom or molecule is convected out of the primary beam before emission occurs. (v) Significant populations of the upper level of an observed transition may result from the de-excitation of higher levels by either radiative or collisional processes. Processes (iv) and (v), in contrast to (i)–(iii), do not produce axisymmetric broadening of the beam, and they are a function of the local flow velocity. The last three of these factors can be eliminated by judicious choice of an appropriate transition to observe as they were in the present study.

To ascertain whether any of the above beam-broadening mechanisms were significant, the radial extent of radiation for the 5016 and 3965 Å lines was determined in the particular tunnel-wall boundary layer we wished to investigate. For these tests, the image of the slit was aligned with the direction of the primary beam; it had dimensions 1·5 mm along the beam, and 0·125 mm in the direction transverse to the beam. The slit was scanned upstream and downstream of the beam centre; and the intensity of both lines was recorded as a function of slit position. The results of these measurements, made at three points in the boundary layer, are shown in figure 5. In this figure, intensity, normalized by the maximum value, is plotted against distance, measured in terms of initial beam diameter, upstream and downstream of the point of peak intensity. Use of an Abel integral scheme was *not* made to deduce the radial intensity distribution. For all the measurements, 95 % or more of the total intensity is found within a diameter of 3·0 mm (four initial beam diameters); and slight spreading of the beam can be observed as the distance from the wall y increases. The number density varies by a factor of ten for the three locations, and no abnormal increase in the fluorescent region is observed. This implies that emission, resulting from secondary electron excitation, is not a problem (i.e. either there are very few secondaries with enough energy to produce excited states, or the free path of the secondaries is of order 1 mm or less). Furthermore, the region of fluorescent emission is essentially the same for the 5016 as for the 3965 Å line. This is desirable, in that the effective spatial (or temporal) resolution of both lines is the same. For these flow conditions and a fluorescent region diameter of 3 mm, (6) shows that the frequency response is of the order 0·5 MHz.

4.3. *Signal-to-noise ratio*

In addition to spatial resolution and frequency response, signal-to-noise ratio is an important consideration. When studying turbulent flows, one is not faced with dark current type noise, but shot noise can be a problem. That is, a sufficient number of photons must be received at the photocathode of the photomultiplier tube in a time corresponding to the period of the maximum observed fluctuation frequency to have a statistically accurate measure of the intensity variation with time. A probable error of less than $\pm 4\,\%$ for a 1 MHz signal requires 10^3 photoelectrons $(\mu s)^{-1}$ from the photocathode. This corresponds to 10^4 photons $(\mu s)^{-1}$ for a photocathode with 10 % quantum efficiency. For our receiving optics, we observed approximately 3×10^3 photons $(\mu s)^{-1}$ at 3965 Å, with a measured signal-to-noise ratio of approximately 20 in the free stream, with a 2·0 mA beam and a 15 kΩ load resistor with 300 kHz frequency response.

The noise level at the mid point of the boundary layer is approximately twice this value. The more intense 5016 Å line, on the other hand, provided a free-stream r.m.s. noise level of 1 % with 300 kHz frequency response. Beam currents of order 10 mA are attainable, and would provide improved signal-to-noise ratios and/or frequency response. Since our present tape recorder frequency response is limited to 40 kHz FM and 300 kHz direct, further attempts to improve this performance were not warranted.

5. Results for an adiabatic wall, hypersonic boundary layer

Measurements were made in the tunnel-wall boundary layer of the He-2 facility at a position 82 cm from the throat. Reservoir conditions were 15·3 atm and 300 °K. Free-stream properties were $M = 16{\cdot}3$, $n = 4{\cdot}41 \times 10^{17}\,\mathrm{cm}^{-3}$, $T = 3{\cdot}5$ °K, $P = 0{\cdot}154$ Torr. The Reynolds number based on free-stream properties and distance from the throat was $4{\cdot}4 \times 10^6$. Re_θ based on momentum thickness determined from mean flow profiles was 1700. Wall pressure and temperature were 0·500 Torr and 300 °K, respectively.

5.1. *Pitot pressure measurements*

Boundary-layer Pitot pressure surveys were made with a $0{\cdot}225 \times 0{\cdot}50$ mm flattened probe, connected to a Pace 2·0 p.s.i. differential pressure transducer referenced to vacuum. The Pitot pressure distribution along with the temperature and density profiles deduced from the measured Pitot pressure and wall temperature and pressure are shown in figure 6. No substantial difference in the density distribution resulted from assuming (i) the static pressure was constant and equal to the wall value, or (ii) the static pressure was constant and equal to the free-stream value. The temperature distribution shows more sensitivity to the choice of static-pressure assumption. The Pitot pressure distribution in figure 6 indicates that a compression region exists near the outer edge of the boundary layer, probably resulting from the compression corner created by the intersection of the axisymmetric nozzle with the flat test-section wall. Thus, we are *not* dealing with a canonical $\partial p/\partial x = 0$ (or $\partial p/\partial y = 0$, for that matter) boundary layer. These results are to be viewed in the spirit that they confirm the validity of the technique, and that they indicate some of the general characteristics to be found in hypersonic, adiabatic wall boundary layers, rather than that they provide a detailed study of a fundamental, easily recognized, equilibrium boundary layer.

It is difficult to define the edge of the boundary layer in this type of flow. Owing to the intermittent nature of the fluctuations observed at distances greater than 2·54 cm from the wall and the sharp peak in the Pitot pressure at this height, a boundary-layer thickness of 2·54 cm has been somewhat arbitrarily assumed.

5.2. *Fluorescence intensity measurements*

For these tests a 20 keV beam of electrons with a nominal beam current of 2 mA emanating from a 1·125 mm dia. hole in the tunnel wall was used to generate the observed fluorescence. To prevent any disturbance by the electron-beam vacuum

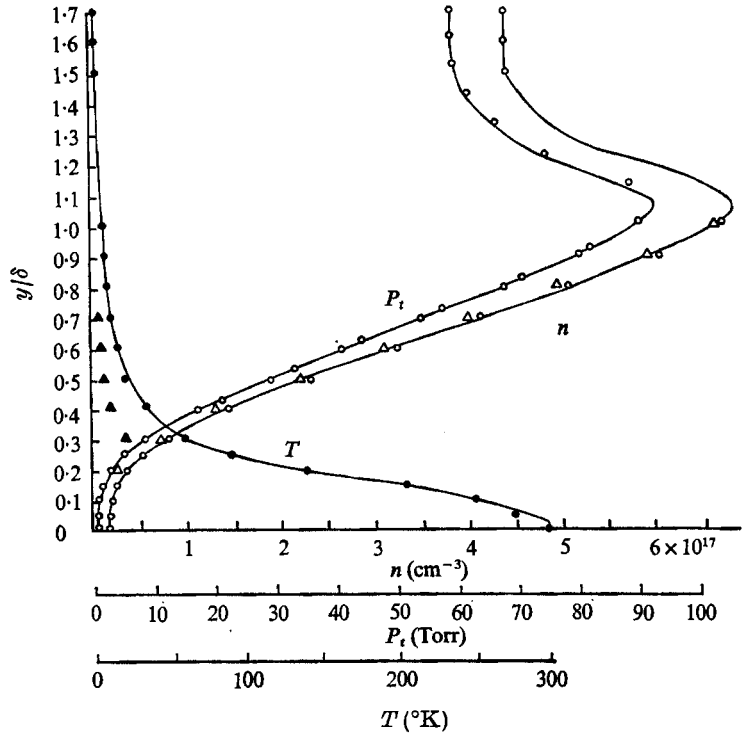

FIGURE 6. Mean Pitot pressure distribution, with calculated mean density and temperature distributions for the (He-2) wall boundary layer. Pitot probe 0·125 mm high. $M = 16$, $P_0 = 225$ p.s.i., $\delta \simeq 2{\cdot}5$ cm. ○, △, n; ●, ▲, T. ○, $P(y) = P_{\text{wall}} = 0{\cdot}500$ Torr; △, $P(y) = P = 0{\cdot}154$ Torr.

pumping system, a small helium bleed was used to maintain the wall pressure at the drift tube entrance at the previously measured wall pressure (Lewis 1970). An example of the intensity variation observed at various locations in the boundary layer is shown in figure 7 (plate 1). Shown here are oscillograms of the photomultiplier tube output monitoring the 5016 Å intensity. These oscillograms were taken with a relatively slow sweep speed (5 m s div^{-1}), to demonstrate the intermittency that exists at both the outer and the inner edge of the turbulent region of the boundary layer. (The oscilloscope sensitivity varies by an order of magnitude from the free stream, $y = 3{\cdot}81$ cm, down to $y = 0{\cdot}254$ cm, so no relative intensity variation from picture to picture is apparent.) As one proceeds from the free stream to $y = 2{\cdot}54$ cm, an occasional burst of low density and/or high temperature is observed, producing a momentary decrease in intensity. At $y = 1{\cdot}778$ cm, the intensity fluctuations appear to be more or less equally distributed about some mean value. And at $y = 0{\cdot}766$ cm, which is near the top of the sublayer (see figure 6), occasional bursts of high-density and/or low-temperature fluid appear, which increases the intensity momentarily. At $y = 0{\cdot}254$ cm, the signal is again relatively smooth. At this location, where the mean density is very low, signal fluctuations for either line can arise only from noise or density fluctuations. Comparison of the time histories for both lines

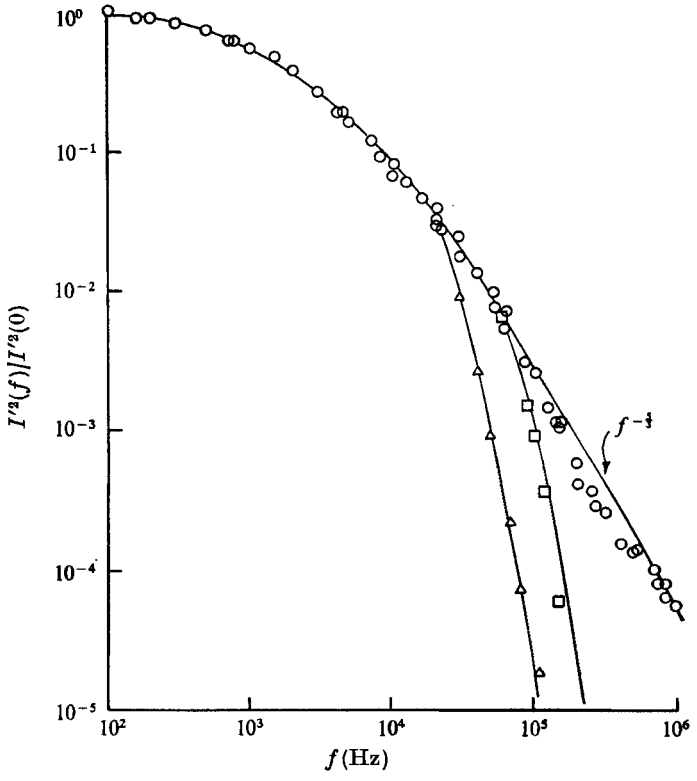

FIGURE 8. Power spectrum of 5016 Å intensity fluctuations at $y/\delta = 0{\cdot}5$. $(R_L C_L)^{-1}$: ○, 1000 kHz (4 $k\Omega$); □, 80 (47); △, 24 (163).

show that the bulk of the fluctuations are not correlated with each other and therefore arise from noise. Thus, the flow at this location is essentially laminar.

The intensity variations of the two lines (5016 and 3965 Å) were measured simultaneously, by recording the voltage fluctuations on the 15 kΩ load resistors on a Honeywell, Model 5600, tape recorder. This recorder provides a bandwidth of d.c. to 40 kHz on FM, and 300 Hz to 300 kHz on direct (AM) record. Though the signals were recorded in the direct-record mode, no analysis of these larger bandwidth recordings has yet been made, because careful restoration of the d.c. components is required to deduce density and temperature time histories. Thus, the results presented here are all limited to the 40 kHz bandwidth of the FM recorder, in spite of the better than 300 kHz bandwidth available from the electron-beam detector assembly.

Some idea of the penalty paid for this reduced bandwidth can be discerned from figure 8. In this figure, the power spectrum of the intensity fluctuations for the 5016 Å light taken at the approximate location of maximum fluctuations ($y = 1{\cdot}27$ cm) is shown. These results were obtained with a Tektronix R564B Storage Oscilloscope with a Type 3L5 Spectrum Analyzer plug-in. Originally they were used to determine the effect on bandwidth of various photomultiplier tube load resistors. One can see that the 40 kHz bandwidth of the tape recorder includes the intensity fluctuations down to the 10^{-2} point of the power spectrum

(i.e. approximately 15 % of the area under the curve is excluded). While this figure does not provide a direct measure of the power spectrum of either density or temperature fluctuations, it is felt to be appropriate for determining the qualitative impact of bandwidth limitations.

The procedure for each run consisted of recording the free-stream intensities *and* beam current at the beginning and the end for approximately 20 s, and recording at various locations in the boundary layer for approximately the same length of time. It was possible to record at as many as seven different points in the boundary layer plus the free stream twice during the 4 or 5 minutes of test time available in a single run.

Digital tapes of the two intensity time histories were then made by playing the analog tapes back into a Datacom Model 8015 Data Acquisition System. The two-channel digital tape contained one second of data (256 000 data points) for each intensity for each point in the flow. These digital tapes were then processed on an IBM 360/91 computer. In generating the digital tapes, care was taken to select portions of the analog tapes in which beam-current fluctuations were less than $\pm 2\,\%$. This rather crude filtering process was necessary because only two FM playback amplifiers were available in our borrowed recorder. A better procedure would be simultaneously to digitize the beam-current signal, and normalize each intensity point during analysis on the 360/91.

The mean and r.m.s. intensity fluctuation profiles were computed directly from the digital tapes. The mean intensity profiles can be extracted from figures 2 and 3. The r.m.s. intensity fluctuation profiles, normalized by the local mean, are shown in figure 9. The r.m.s. variations in the 5016 Å signal are seen to increase from a minimum of 1 % in the free stream to 50 % at $y/\delta = 0{\cdot}3$. The level of 3965 Å fluctuations increases from 7 % in the free stream to 40–50 % at $y/\delta = 0{\cdot}3$. Much of the 3965 Å signal fluctuations at $y/\delta < 0{\cdot}3$ can be attributed to shot noise. Since the mean 3965 Å signal near the wall is an order of magnitude lower than the free-stream value, the expected shot noise near the wall will be $\sqrt{10}$ larger than the 7 % observed in the free stream. By contrast, shot noise associated with the 5016 Å signal near the wall is of the order of 5 %.

Two important features of hypersonic adiabatic wall boundary layers can be observed from the fluorescent intensity data in figures 7 and 9. (i) Fluctuations are large and can be very 'one-sided' in the intermittent regions near the edges of the turbulent layer. (ii) The r.m.s. sublayer occupies a significant fraction of the total boundary-layer height, approximately 20–30 % in the boundary layer studied here. The first characteristic leads to the possibility of very asymmetric probability distributions with fluctuations that are large compared with the local mean. The second characteristic leads one to think of these boundary layers as having a turbulent middle region with a relatively thick, low density, high-temperature, essentially laminar region next to the wall.

5.3. *Mean flow profiles*

In the data reduction scheme on the 360/91, free-stream average intensities were used to generate the values of c_1 in (2) for each line. The temperature coefficient α was assumed to be $\frac{1}{3}$ for both intensities, since this greatly reduced execution

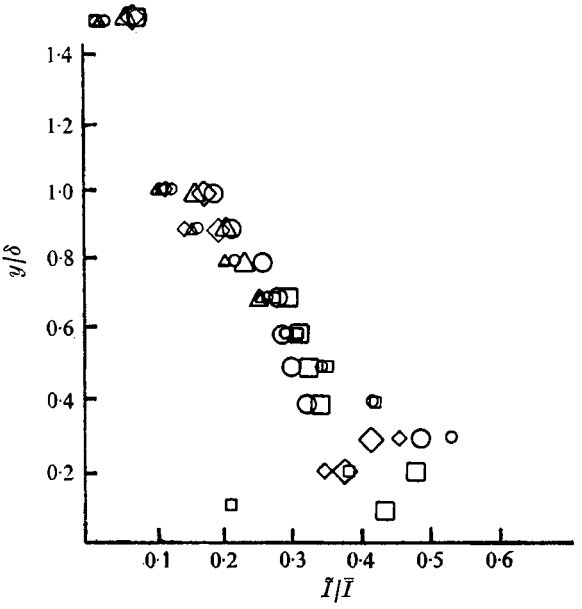

FIGURE 9. Normalized distributions of the r.m.s. of fluctuations in intensity $\tilde{I}/\bar{I}$ against distance from the wall y/δ.

Run	13	14	15	17
5016 Å	○	□	△	◇
3965 Å	○	□	△	◇

time. The appropriate values of c_2 giving the best least-squares fit to the calibration data were used in the data reduction scheme. Thus, the value of c_2 used for the 3965 Å line differs slightly from the value given in table 1. Mean and r.m.s. values were then computed by taking the appropriate averages of the calculated values at each point in the boundary layer.

The distributions of the mean density, temperature and pressure are shown in figures 10–12, respectively. Also shown are the mean density and temperature profiles deduced from the Pitot pressure measurements as described in the discussion of figure 6. Several features can be noted from these figures. First, the scatter in the data appears greatest in the density and temperature profiles in those regions where the technique loses sensitivity to that particular flow variable. For example, for $y/\delta > 0{\cdot}9$ in this particular boundary layer, the error in determining density should be approximately five times larger than the errors associated with measuring the two line intensities. The mean pressure profile, resulting from averaging the instantaneous products of density and temperature, of course, shows greater scatter at both ends. Second, the data appear to have scatter resulting from run-to-run variations. This is felt to be the result of using the free-stream conditions to determine the values of c_1 from (2). Since density sensitivity in the free stream is relatively poor, small variations in tunnel conditions, in electron-beam current, or small errors in the tape recorder gains or d.c. offset (which were calibrated before recording and playback) could produce systematic differences of several per cent between different runs.

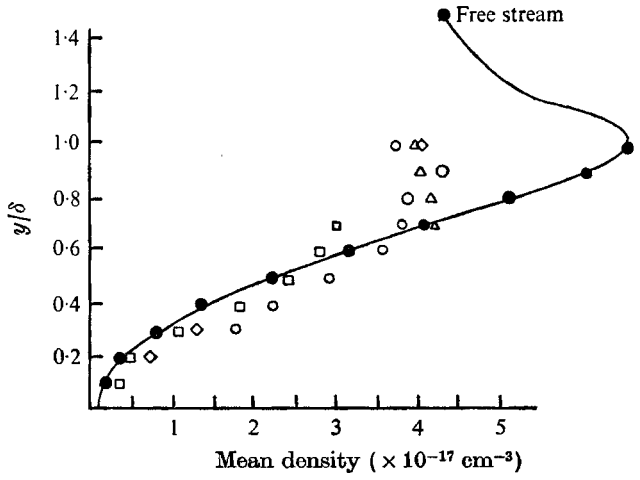

FIGURE 10. Mean density distribution in the boundary layer. Distance from the wall y/δ. ●, from Pitot data.

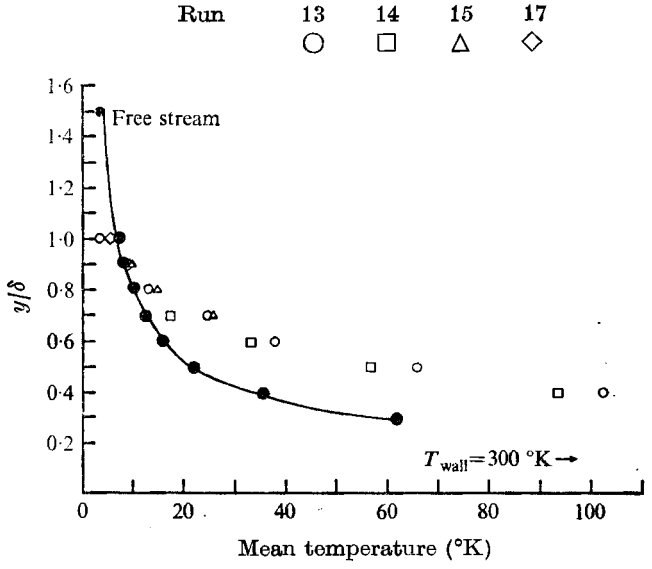

FIGURE 11. Mean temperature distribution in the boundary layer. Distance from wall y/δ. $\delta \simeq 2{\cdot}5$ cm. Symbols as for figure 10.

Figure 10 shows that the mean densities determined by the fluorescence technique agree well with those determined by Pitot surveys in the region where the former technique is most sensitive. The lack of agreement in the outer portion of the flow may arise from low density sensitivity of the fluorescence method. Mean density and pressure values for $y/\delta \leqslant 0{\cdot}3$, shown in figures 10 and 12, were computed by assuming an average temperature at each location and computing the time variation of density from the intensity fluctuations measured for the 5016 Å line. Mean densities computed in this manner were not sensitive to the choice of this assumed average temperature. For example, at $y/\delta = 0{\cdot}1$, using an assumed temperature of 150 instead of 250 °K changes the mean density by

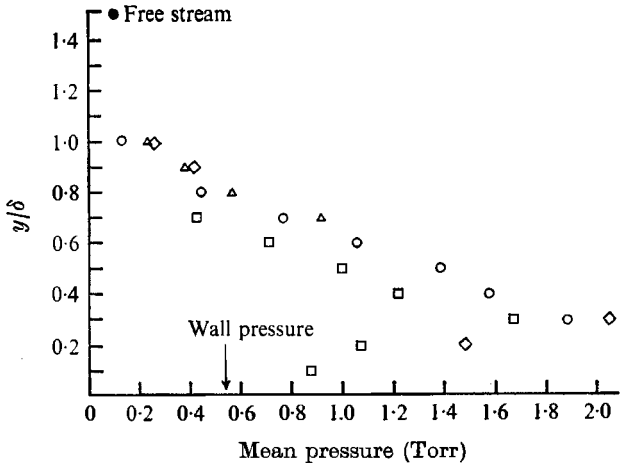

FIGURE 12. Mean pressure distribution in the boundary layer. Distance from wall y/δ. $\delta \simeq 2{\cdot}5$ cm. Symbols as for figure 10.

only 10%. The mean pressures, on the other hand, will vary approximately linearly with the assumed average temperature. To minimize the error the average temperature employed came from an extrapolation of the mean temperature at $y/\delta = 0{\cdot}4$ to the wall value, 296 °K. Reasonable agreement with the respective wall values determined from wall temperature and Pitot pressure measurements can be observed.

Figure 11 shows that the mean temperatures determined from the fluorescence technique are all larger than the mean temperatures predicted from the Pitot surveys. A possible cause of this apparent large difference is discussed later.

5.4. *Fluctuation level distributions*

The r.m.s. of the fluctuations in density, temperature and pressure, computed from the intensity time histories, are shown in figures 13–15, respectively. The normalized r.m.s. density fluctuation distribution shown in figure 13 was computed by averaging over each file of data:

$$\frac{\tilde{n}}{\overline{n}} = \frac{\left[N^{-1}\sum_{j=1}^{N}(n_j^2 - \overline{n}^2)\right]^{\frac{1}{2}}}{\overline{n}}.$$

n_j, $\overline{n}$ and N are, respectively, the instantaneous density, mean density and total points in the file (~ 250000).

The distribution of density fluctuation levels shown in figure 13 is similar to hot-wire results obtained in other hypersonic adiabatic wall boundary layers. Kemp & Owen (1972) report that r.m.s. mass flow fluctuations $\widetilde{\rho u}/\overline{\rho u}$ peak at 0·80 at $y/\delta = 0{\cdot}4$ in the Mach 38 boundary layer they studied; a strong 'one-sided' intermittent signal was noted at this location. Fischer *et al.* (1971) measured peak mass flow fluctuations of 0·50 at $y/\delta = 0{\cdot}4$ in a Mach 20 adiabatic wall boundary layer. Laderman & Demetriades (1974) and Owen & Horstman (1974) presented results which indicate that velocity fluctuations in hypersonic

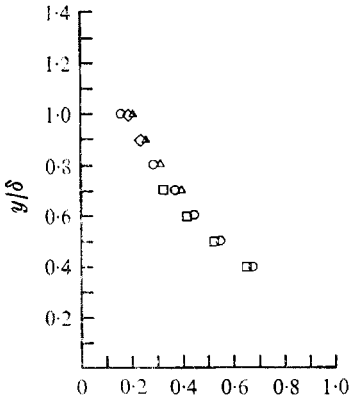

FIGURE 13

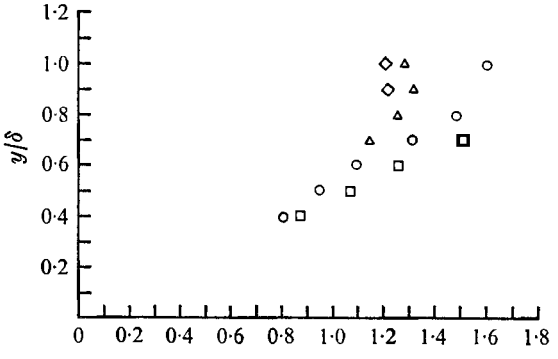

FIGURE 14

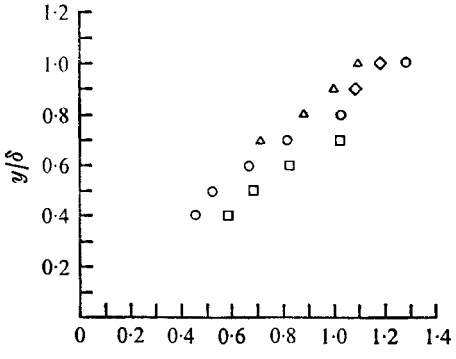

FIGURE 15

FIGURE 13. Normalized distribution of the r.m.s. of fluctuations in density against distance from the wall y/δ. $\delta \simeq 2{\cdot}5$ cm. Symbols as for figure 10.

FIGURE 14. Normalized distribution of the r.m.s. of fluctuations in temperature against distance from the wall y/δ. $\delta \simeq 2{\cdot}5$ cm. Symbols as for figure 10.

FIGURE 15. Normalized distribution of the r.m.s. of fluctuations in pressure against distance from the wall y/δ. $\delta \simeq 2{\cdot}5$ cm. Symbols as for figure 10.

turbulent boundary layers are small compared with fluctuations in the thermodynamic state variables. Therefore, the mass flow fluctuation levels determined from hot-wire measurements should be similar to the density fluctuation levels determined in the present study. Fluctuation levels for $y/\delta \leqslant 0{\cdot}3$ are not shown in figure 13. However, an estimate of their magnitude can be determined from the normalized r.m.s. fluctuation levels of the 5016 Å line intensity shown in figure 9. In this region, the 5016 Å intensity is essentially a function of density, becoming linearly proportional to density as the wall is approached. From figure 9 we deduce that the normalized r.m.s. density fluctuation levels decrease from their maximum of 0·65 at $y/\delta = 0{\cdot}4$ to a value of less than 0·20 at $y/\delta = 0{\cdot}1$.

The normalized r.m.s. temperature fluctuation levels shown in figure 14 exceed 1·00 near the outer edge of the boundary layer, and decrease as one approaches

the wall. In viewing figure 14, one must keep in mind that the mean temperature is very small near the outer edge (e.g. $\overline{T} = 5{\cdot}0\,^{\circ}\mathrm{K}$ at $y/\delta = 0{\cdot}8$), and increases by two orders of magnitude at the wall. Laderman & Demetriades (1974) also observed maximum normalized temperature fluctuations near the outer edge of their $M = 9{\cdot}4$ boundary layer. It might be more appropriate to normalize the fluctuation levels by the mean temperature difference across the layer. The reason for the appearance of $\tilde{T}/\overline{T} > 1{\cdot}00$ will be apparent from the probability density distributions to be discussed in § 5.5.

The profile of r.m.s. pressure fluctuations normalized by the local mean is shown in figure 15. Mean and r.m.s. pressure fluctuation results are more sensitive to errors in the measuring technique than are density and temperature results since the instantaneous pressure is the product of n and T, which accumulates the errors in each. Despite some uncertainty, it is clear from figure 15 that pressure fluctuation levels are not negligible compared with those of other thermodynamic state variables. This result has important implications for theoretical and experimental studies of hypersonic turbulent flows in which the no-sound ($\tilde{P}/\overline{P} \simeq 0$) assumption is often invoked.

5.5. *Probability density distributions*

The one-sided intensity fluctuations shown in figure 7, and the normalized temperature and pressure fluctuation levels shown in figures 14 and 15, indicate that fluctuations are often not symmetrically distributed about a mean value. This is not too surprising, in view of the large gradients in mean flow properties that exist in the boundary layer studied. Probability density distributions were constructed from the density and temperature time histories computed from the fluorescence data. Shown in figures 16 and 17 are probability density distributions at several points in the boundary layer for density and temperature, respectively. These are shown as continuous curves since each curve is comprised of from 100 to 240 points or cells. The cell size for the density probability density curves was $\Delta n = 0{\cdot}80 \times 10^{16}\,\mathrm{cm}^{-3}$ (i.e. a probability of 0·01 at a particular density in figure 16 implies that there is a 1 % probability of finding the density within $\pm 0{\cdot}4 \times 10^{16}\,\mathrm{cm}^{-3}$ of that particular density). The cell size for the temperature distributions is $\Delta T = 0{\cdot}25\,^{\circ}\mathrm{K}$. Approximately 150 000 data points were examined to construct each histogram.

In figure 16 it can be observed that the density fluctuations are approximately symmetrically distributed about the mean for $y/\delta \geqslant 0{\cdot}7$. The high-density portions of these curves may be artificially clipped by the lack of density sensitivity of the fluorescence technique in this region. However, the profile of mean density, deduced from the Pitot pressure, indicates a nearly linear profile, which would tend to produce a symmetric fluctuation distribution. As one proceeds towards the wall, more and more low-density fluid, mixed from below, is observed; the probability density distribution becomes very broad, and essentially flat at $y/\delta = 0{\cdot}5$. Intensity fluctuations were observed to be symmetrically distributed about the mean at this location also. As the intermittent region at the bottom edge of the boundary layer is approached ($y/\delta = 0{\cdot}4$), the probability density distribution becomes more peaked with a relatively large high density tail. This

is the location for which the maximum r.m.s. density fluctuation levels were observed; and it is clear why this is so, in that the mean density is approximately double the most probable density.

The temperature probability density distributions displayed in figure 17 are quite different from those for density arising from the differences in the mean profiles (figures 10 and 11). These show the evolution from highly-skewed distributions to very broad, more nearly symmetric distributions, as the wall is approached. Such trends are consistent with the curvature of the mean temperature distribution shown in figure 11. The limited temperature sensitivity of this technique precluded the construction of probability density distributions for $y/\delta < 0{\cdot}4$. It is predicted that a probability density distribution, skewed to the left, would be observed very close to the wall. It is clear from figure 17 why r.m.s. temperature fluctuation levels exceed the mean, in view of these highly-skewed probability distributions.

5.6. *Comparison of fluorescence and pitot probe results*

The mean density distributions shown in figure 10, deduced from the fluorescence and Pitot pressure measurements, agree well over most of the boundary layer. The discrepancy that exists for $y/\delta > 0{\cdot}8$ is probably the result of poor density sensitivity of the fluorescence technique in this region. In view of the large density fluctuation levels observed in the middle of the boundary layer, it might at first be surprising that the Pitot pressure results provide such an accurate mean density distribution. There are two factors responsible for this good agreement. The first is that, in a hypersonic flow such as this, the instantaneous Pitot pressure is approximately

$$P_t = (\text{const.})\,\rho u^2. \tag{7}$$

Thus, the mean Pitot pressure $\overline{P}_t$ can be related to the mean and fluctuating components of density and velocity by

$$\overline{P}_t \sim \overline{\rho}(\overline{u})^2\left[1+\frac{\overline{u'^2}}{\overline{u}^2}+\frac{\overline{2\rho'u'}}{\overline{\rho u}}+\frac{\overline{\rho'u'^2}}{\overline{\rho u}^2}\right]. \tag{8}$$

(The quantities with bars indicate mean values, and primes indicate fluctuating components.) For locations near the outer edge of the boundary layer, the fact that the density fluctuations were observed to be distributed symmetrically about the mean, that the velocity fluctuations were small, and that the velocity was essentially equal to the free-stream value leads one to conclude that it may be possible to construct a reasonable mean density profile from time-averaged Pitot pressure measurements. Another way of saying this is that the agreement between the mean density profiles determined by the two techniques (shown in figure 10) indicates that the sum of the correlation terms inside the square brackets of (8) is small.

The comparison between the mean temperature results, derived from the two techniques (shown in figure 11), is not nearly as favourable. In fact, it appears that the temperatures deduced from the Pitot pressure more nearly equal the *most probable* temperatures derived from the probability density distributions shown in figure 17. This is an example of the difficulties, alluded to in § 1, in

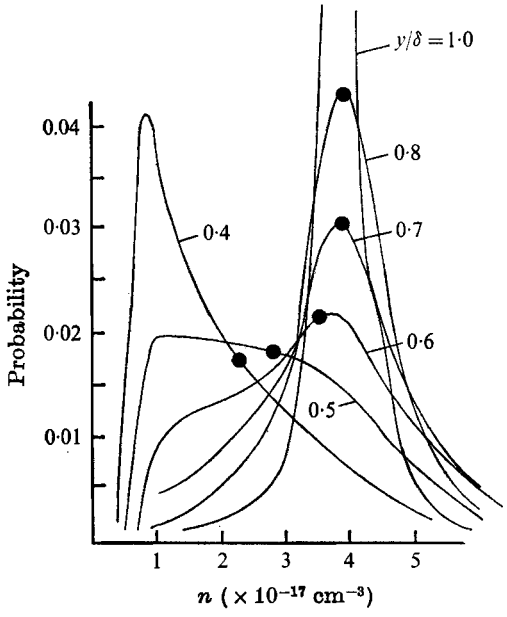

Figure 16. Probability density distributions for density at various locations in the boundary layer. Run 13. ●, $\bar{n}$.

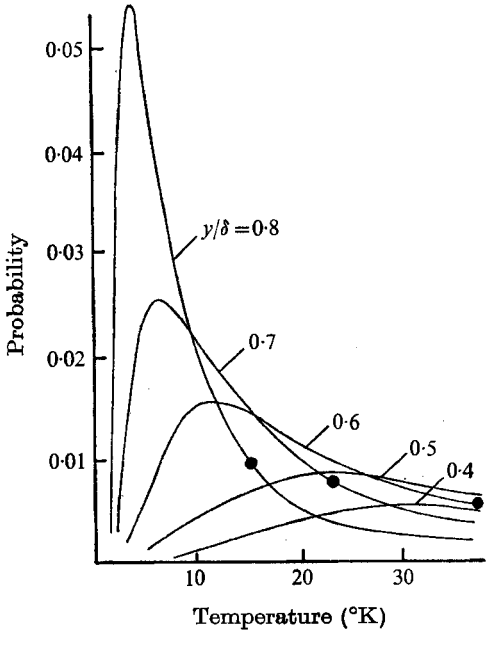

Figure 17. Probability density distributions for temperature at various locations in the boundary layer. Run 13. ●, $\bar{T}$.

extracting mean flow properties from a time-average probe response, which is a function of several variables with large, asymmetrically distributed fluctuations. Even if time-resolved Pitot pressure measurements were available, it is doubtful whether an accurate mean temperature distribution could be constructed without additional simultaneous measurements.

6. Conclusions

From these initial measurements, one may draw the following conclusions. (i) The electron-beam fluorescence technique has been established as a means of measuring density, temperature, as well as other thermodynamic state variable fluctuations in compressible turbulent flows. The technique is primarily limited by electron-beam operation at high number densities, and by the sensitivity of fluorescence intensity to the flow quantities of interest. (ii) The fluctuations in density, temperature and pressure observed in this hypersonic adiabatic wall boundary layer have been shown to be large. They are so large, and in many cases asymmetrically distributed about the mean, that a linearized treatment of them is impossible. (iii) In contrast to observations in low supersonic Mach number boundary layers, the pressure perturbations observed in the present study are too large for one to be able to neglect them in any theoretical treatment. Additional analysis of these data, to determine power spectra and correlations, as well as additional measurements at higher stagnation pressures (increased Reynolds numbers), is to be performed in the future.

The authors wish to acknowledge the many helpful discussions they had with F. R. Hama. His advice and encouragement were very valuable in this investigation. Assistance from R. Bogart in running the wind tunnel, G. Katona in setting up the electron beam and related electronics, and R. Gilbert in setting up the data reduction scheme is gratefully acknowledged. This work was supported by the Air Force Office of Scientific Research under contract F44620-71-0032.

REFERENCES

Boyer, A. G. & Muntz, E. P. 1967 *AGARD Current Paper*, no. 19, vol. 2.

Driscoll, J. F. 1975 Ph.D. thesis, Princeton University.

Fischer, M. C., Maddalon, D. V., Weinstein, L. M. & Wagner, R. D. 1971 *A.I.A.A. J.* **9**, 826.

Hilliard, M. E., Ocheltree, S. L. & Storey, R. W. 1970 *N.A.S.A. Tech. Note, D*-6005.

Hunter, W. W. 1972 Ph.D. thesis, Virginia Polytechnic Institute.

Kemp, J. H. & Owen, F. K. 1972 *N.A.S.A. Tech. Note, D*-6965.

Laderman, A. J. & Demetriades, A. 1974 *J. Fluid Mech.* **63**, 121.

Lewis, J. H. 1970 Ph.D. thesis, Princeton University.

Lin, C. C. & St John, R. M. 1962 *Phys. Rev.* **128**, 1749.

Maguire, B. L. 1967 *Rarefied Gas Dynamics*, vol. 2, suppl. 4 (ed. C. L. Brundin), p. 1497. Academic.

Massey, H. S. W. & Burhop, E. H. S. 1969 *Electronic and Ionic Impact Phenomena*, vol. 1, p. 203. Oxford University Press.

Mitchell, A. C. G. & Zemansky, M. W. 1971 *Resonance Radiation and Excited Atoms*, p. 192. Cambridge University Press.

MUNTZ, E. P. 1968 *AGARDograph*, no. 132.

MUNTZ, E. P. & MARSDEN, D. J. 1963 *Rarefied Gas Dynamics*, vol. 2, suppl. 2 (ed. J. A. Laurmann), p. 495. Academic.

OWEN, F. K. & HORSTMAN, C. C. 1974 *A.I.A.A. Preprint*, no. 74–93.

ST JOHN, R. M., BRONCO, C. J. & FOWLER, R. G. 1960 *J. Opt. Soc. Am.* **50**, 28.

WALLACE, J. E. 1968 *N.A.S.A. Special Paper*, no. 216.

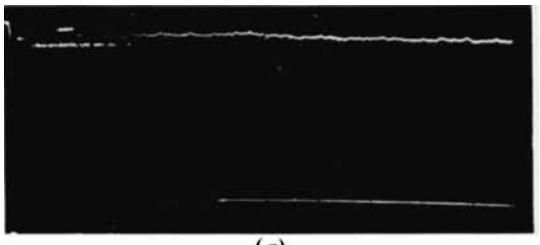

(*a*)

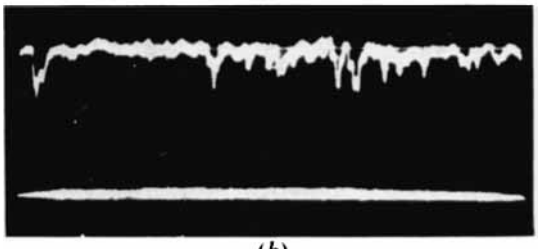

(*b*)

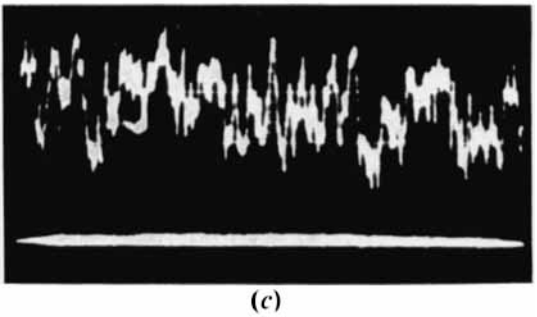

(*c*)

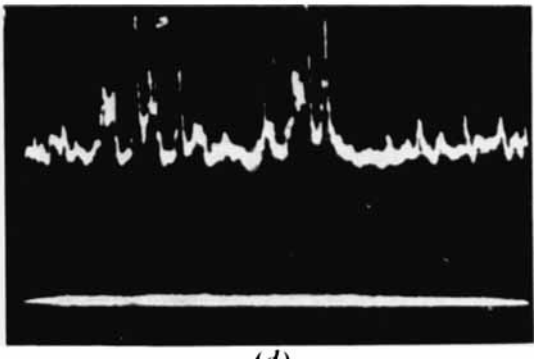

(*d*)

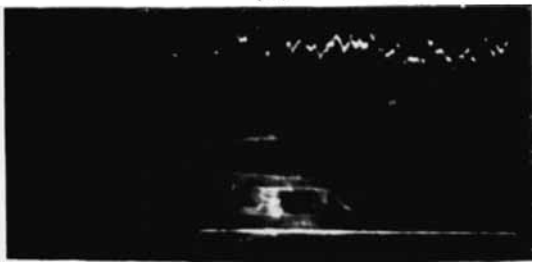

(*e*)

FIGURE 7. Representative intensity variations with time for the 5016 Å line at various points in the boundary layer. 5 ms div^{-1}. (*a*) Free stream (y = 3·81 cm); (*b*) intermittent (2·54); (*c*) turbulent (1·78); (*d*) intermittent (0·76); (*e*) viscous sublayer (0·25).